Article

Principles Determining the Structure of Transition Metals

Samuel K. Riddle [1,2], Timothy R. Wilson [1,2] Malavikha Rajivmoorthy [1,3] and M. E. Eberhart [1,2]*

[1] Molecular Theory Group, Colorado School of Mines, USA
[2] Department of Chemistry, Materials Science Program, Colorado School of Mines, USA
[3] Department of Metallurgical and Materials Engineering, Colorado School of Mines, USA
* Correspondence: meberhar@mines.edu

Abstract: For the better part of a century researchers across disciplines have sought to explain the crystallography of the elemental transition metals: hexagonal close packed, body centered cubic, and face centered cubic in a form similar to that used to rationalize the structure of organic molecules and inorganic complexes. Pauling himself tried with limited success to address the origins of transition metal stability. These early investigators were handicapped, however, by incomplete knowledge regarding the structure of metallic electron density. Here we exploit modern approaches to charge analysis to first comprehensively describe transition metal electron density. Then, we use topological partitioning and quantum mechanically rigorous treatments of kinetic energy to account for the structure of the density as arising from the interactions between metallic tetrahedra. We argue that the crystallography of the early transition metals results from charge transfer from the so called "octahedral" to "tetrahedral holes" while the face centered cubic structure of the late transition metals is a consequence of anti-bonding interactions that increase octahedral hole kinetic energy.

Keywords: Quantum Theory of Atoms in Molecules; Viral Theorem; Frontier Orbital Theory; Variational Principle; Transition Metal Structure

1. Introduction

1.1. Historical Motivation

One can not help but be struck by how little metallurgical thought has been impacted by the century long advances to the conceptual and theoretical framework of molecular chemistry. Where this framework can be applied it provides the insights necessary to design molecules and condensed phase systems. Included in the advances contributing to this framework are those derived from valence bond theory [1], frontier orbital theory [2], conservation of orbital symmetry [3], transition state theory as interpreted within the intuitive approach afforded by the Hammond postulate [4], and the application of catastrophe theory through the formalism of the quantum theory of atoms in molecules (QTAIM) [5]. Though these concepts provide many of the theoretical underpinnings of modern chemistry, they are rarely applied to metallurgical research. We do not believe that the reason for this disparity is that molecular chemistry has little to offer metallurgy. Rather, the two disciplines evolved subject to different selective pressures.

On the one hand, the path that led to the development of modern chemistry arguably began with the 1916 work of Lewis [6], a path to which chemists were fully committed by 1939 with the publication of Pauling's definitive text, *The Nature of the Chemical Bond* [1]. This text ensconced chemistry as the science of reactivity. The fact that chemical reactions were driven by electron rearrangement had become part of the chemical zeitgeist by 1923 (if not sooner) when Lewis recognized bases and acids as electron pair donors and acceptors [7]. As a result, for chemists of the time, the distribution and response of electrons became the central element of a science devoted to the study of chemical reactions. The actual arrangement of atoms that afforded this response was a byproduct of their investigations. Between 1940 and roughly the mid 1970s, chemistry made tremendous advances through deeper insights into the nature of electron redistribution resulting from a chemical or physical process. (Each of the great advances mentioned in the preceding paragraph occurred in this time period.) During the subsequent years, first principle methods became

 doi:10.20944/preprints202107.0512.v1

an increasingly important chemical tool, and though these methods ultimately provided the ability to calculate molecular energies and geometries, their initial utility was derived from the expanded insights they provided toward understanding the electron redistribution driving chemical reactions.

On the other hand, modern metallurgy is concerned with atomic arrangements and the energy of these arrangements. In the early part of the twentieth century metallurgical phenomena in which charge rearrangement plays an important role were still not understood. For example, in 1934, Taylor, Orowan and Polanyi [8–10] began individually to zero in on the dislocation as the mechanism of plasticity. Their arguments were based largely on continuum elasticity theory, which is applicable sufficiently far from a dislocation core. However, the energy necessary to displace atoms and create a dislocation (or any defect) fell outside the scope of elasticity theory. Hence, dislocation core energies became a needed parameter in the characterization of slip. Though the resulting elasticity based models were parameter reliant, they provided tremendous metallurgical insight and thus simultaneously made the characterization of atomic arrangements about defects and their corresponding energies a necessary metallurgical goal. Against this backdrop, the utility of maturing first principle methods was judged by their ability to calculate atomic positions and corresponding energies.

This brings us to the current era where through density functional theory (DFT) [11] it is known that the energy of an atomic system, and all properties that depend on the energy, is determined by the electron density. Chemists take this theory, and the computational tools that it spawned, as an affirmation of their original impulse to study the density and its response. Metallurgists see the density as a stepping stone to calculate atomic positions and their energies.

An interesting question arises as to whether it is possible to combine the many tools and formalisms evolving over the last century to construct models of metallurgical structure that lend themselves to a "chemically" based theory of charge rearrangement in metals and alloys. Such a theory would perhaps allow us to apply the tools of molecular chemistry toward a better understanding of phenomena important in the design of metals and alloys. Such an aspiration is beyond the scope of any single study. However, knowing where electron density resides is obviously necessary before one can investigate the response of the density to perturbation. Accordingly, in this paper we investigate the electron density distribution for the fundamental metallurgical structures, body centered cubic (BCC), face centered cubic (FCC) and hexagonal close packed (HCP) and take the first steps in the development of a framework to account for these distributions.

1.2. Background

Today it is a routine matter to calculate ground state crystal structures of fairly complex alloys, and it is a trivial matter to determine the elemental transition metal structures. The results of these calculations are often rationalized in terms of orbital parameters and distributions, e.g., electronic density of states and one electron band energies, see for example the excellent reviews provided in references [12] and [13].

However, there is a rich history associated with attempts by metallurgists and chemists to rationalize the stability of the pure metals as a manifestation of their electronic electron density. In particular, as there are only a few exceptions where the elemental transition metals do not adopt one of three structures BCC, FCC, or HCP, Figure 1, early attempts were directed toward accounting for features of the electronic structure that stabilized each of these structures.

Pauling proposed that interatomic forces in metals could be rationalized from a resonating-valence-bond perspective [14]. Ten years subsequent, Pauling generalized his approach and directly addressed the issue of crystal structure [15]. In the decade following Pauling's investigations, Altmann et al. [16] employed directed valence bond approaches in an attempt to explain the preferred crystal structure of the non-magnetic transition metals. At nearly the same time, Engel and subsequently Brewer [17], based largely on

Preprints (www.preprints.org) | NOT PEER-REVIEWED | Posted: 22 July 2021 doi:10.20944/preprints202107.0512.v1

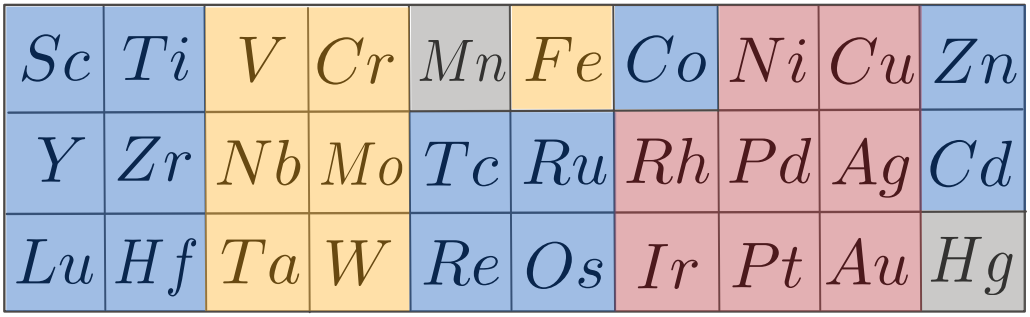

Figure 1. Of the transition metals only Mn and Hg do not possess one of the three crystallographic structures HCP (blue), BCC (orange) or FCC (red) as ground state structures.

correlations, suggested that the spherically averaged number of valence *s*-*p*–electrons was the determining factor favoring one metal structure over another. This model, though it survives to this day, was seen as deficient as it assumed *d*-electrons were inconsequential in mediating crystal structure [18]. Along the same lines, other investigators noted a correlation between preferred crystal structures and electrons to atom ratios, e/a [19].

These early attempts to associate crystalline stability with features of the electron density were handicapped by a lack of knowledge regarding the actual electron density associated with a particular crystal structure. With the tools now available we are no longer so handicapped and can revisit these early investigations with a fresh modern approach toward describing the electron density.

1.3. The Structure of the Electron Density

A general method of classifying the structure of the electron density—a 3D scalar field—is in terms of its topology, which is fully determined by it extremal points, i.e., the points where the density achieves maximal, minimal, or saddle behavior with respect to neighboring points.

Extremal points are the common critical points (CPs) of Morse Theory [20], and in 3D fields must be either maxima, minima, or one of two kinds of saddle point. These CPs are distinguished by an index giving the number of principal positive curvatures minus the number of principal negative curvatures of the field variable at this point. For example, at a minimum the electron density curves up (positive) in all directions and obviously also up in the three principal direction; therefore it is called a +3 CP. A maximum is denoted as a -3 CP, because all three curvatures are negative. The two remaining CPs are designated +1 and -1.

CPs have a special relationship to molecular structure [5,21]. For instance, the electron density at an atomic nucleus is always a maximum, +3 CP; and hence it is also called a nuclear CP. Though the existence of non-nuclear maxima was discussed as early as 1955 [22] it was much later that the first such points were discovered in silicon crystals [23,24] and of relevance to this article in the early HCP metals [25]. Such CPs are designated non-nuclear attractors (NNA) or pseudo-atoms.

The other CPs give information about the way maxima are connected. The simplest and perhaps most significant of these connections originates at the -1 CP and terminates at a nuclear CP, which in general lies along a electron density ridge. This path has the topological properties one would expect of a chemical bond. And hence motivated studies showing its presence between nuclei that conventional wisdom assumed to be bound [5,24, 26]. Therefore, this ridge is descriptively referred to as a bond path and the accompanying -1 CP as a bond CP. Other types of CPs emerge as chemically meaningful as the connections between nuclei take on additional topological characteristics. A +1 CP is required at the center of ring structures (rings of bond paths), and is designated as a ring CP. Cage structures must enclose a single +3 CP and are given the name cage CPs [27].

Preprints (www.preprints.org) | NOT PEER-REVIEWED | Posted: 22 July 2021 doi:10.20944/preprints202107.0512.v1

Associated with the nuclear and cage CPs are unique energetically well-defined volumes known as Bader atoms and electronic basins respectively [5,28–30]. For crystals having one symmetry unique atom per unit cell, the Bader atom is nothing more than the familiar Wigner-Seitz cell [24]. The shape of this cell is strictly determined by crystallographic symmetry, however its topology and hence structure is mediated by the types of CPs on its surface.

2. Materials and Methods

The electron density topologies and geometries for each of the 22 non-magnetic transition metals in columns 3-11 of the periodic table—each in the BCC, FCC, and HCP geometries—were determined using the commercial codes BAND [31,32] and VASP [33,34], as well as an in-house research code using a linearized augmented Slater-type orbital basis set (LASTO) [35]. In general, electron density topology is robust and insensitive to variations in lattice constant up to about 10%, code type (VASP, BAND, or LASTO), k-point mesh, basis set size beyond some reasonable value, and choice of density functional. The results shown here, unless otherwise noted, are the BAND results employing a triple zeta basis set with polarization and the Vosko, Wilk, and Nusair local density approximation [36] and employing the zero order regular approximation (ZORA) for relativistic effects [37].

Topological partitioning of the electron density was performed using the in-house developed Bondalyzer [38] addons, and the Tecplot [39] modeling suite. Each atomic basin was partitioned using Gradient Bundle Analysis (GBA), employing 20,000 gradient bundles per atom, and no adaptive mesh subdivision. Integrated values for electron density and kinetic energy in topological cages corresponding to the crystallographic holes were then found. Average values for kinetic energies in the tetrahedral and octahedral holes for each atom are reported.

3. Results

The electron density topology of crystals having one symmetry unique atom per unit cell is captured by specifying the boundaries of the Wigner-Seitz cell, the locations and types of CPs contained in and on the cell, and the bond paths connecting the nuclear CPs of neighboring cells. Such representations are given in Figure 2 for the four observed ground state topologies characteristic of the 22 non-magnetic transition metals.

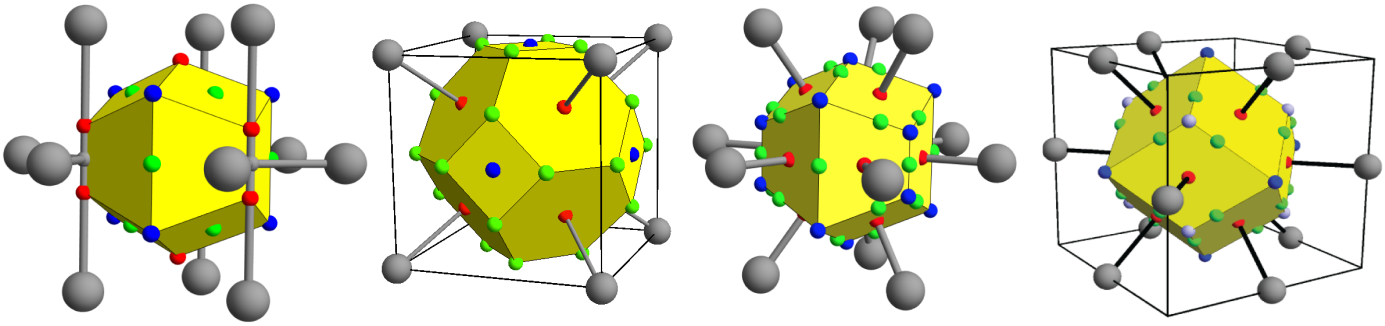

Figure 2. From left to right the topology of the non-magnetic transition metals of: the early HCP metals of columns 3 and 4; the BCC metals of columns 5 and 6; the late HCP transition metals of columns 7 and 8; and the FCC metals of columns 9, 10 and 11. The yellow polyhedra are the boundaries of the Wigner-Seitz cell about a central atom. The large gray spheres mark the locations of the atoms in the first coordination sphere. Throughout this paper small grey, red, green, and blue spheres denote pseudo atom, bond, ring, and cage CPs respectively. Bond paths connecting the first coordination sphere to the central atom are shown as rods.

For the nonmagnetic transition metals, the crystallographic HCP structure is characterized by two topologies [25], one for the early HCP metals in columns 3 and 4 of the periodic table and the other for HCP metals of columns 7 and 8. The early HCP (*e*HCP) electron density is absent atom-atom connections; rather, all bond paths pass through pseudo-atom

Preprints (www.preprints.org) | NOT PEER-REVIEWED | Posted: 22 July 2021 doi:10.20944/preprints202107.0512.v1

CPs. This pseudo-atom is bound to five early transition metal atoms, requiring bond critical points at the center of HCP tetrahedral hole and cage CPs in the octahedral holes. The crystallographic BCC structure is characterized by eight bond paths to nearest neighbors, a cage CP at the center of the BCC octahedral hole, and a ring CP at the center of the BCC tetrahedral hole. The late HCP (*l*HCP) charge density, as well as the FCC electron density, is as typically conveyed in ball and stick models—each atom is connected to its twelve nearest neighbors via bond paths that produce tetrahedral and octahedral cage CPs in the respective crystallographic holes.

A striking characteristic of these topologies is that while the crystallographic octahedral hole of all structures hosts a cage CP, the character of the CP at the center of the crystallographic tetrahedral holes depends on the structure—appearing as a bond (for *e*HCP), ring (for BCC), or cage CP (for *l*HCP and FCC). This observation invites the question as to whether this topological variation is due to the atoms involved or simply a response to the crystallographic structure. This question may be enlightened by forcing all the non-magnetic transition metals into a common crystallographic structure—BCC, FCC, or HCP—to determine if the resultant topology of these "forced" structures is the same for all transition metals. Accordingly, the electron density was determined for all of the non-magnetic transition metals constrained to each of the BCC, FCC and HCP crystallographic structures. The resultant topologies for the forced BCC structures are represented in Figure 3.

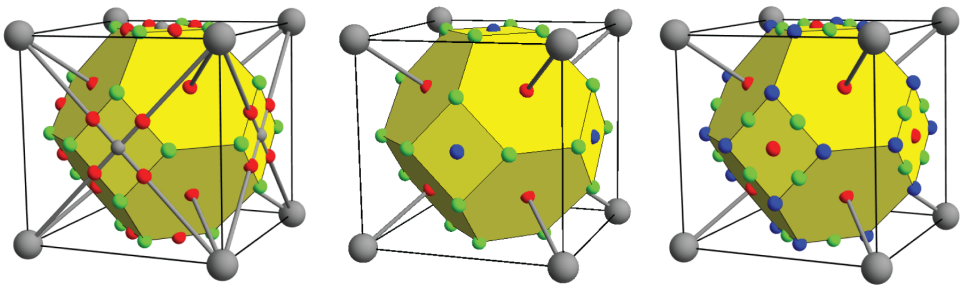

Figure 3. For clarity all the critical points and bond paths of each topology may not be shown. From left to right the topologies of the nonmagnetic early HCP, BCC, and late HCP and FCC metals forced to the BCC crystallographic structure.

Only one forced BCC topology is observed for all the *e*HCP metals (columns 3 and 4) though with electron density nearly flat around several sites (see Figure 4) topological identification is difficult. Nonetheless, it appears that for these metals there is a pseudo-atom CP at the center of the octahedral hole. Bond paths connecting second and third neighbors intersect at these pseudo-atoms. The crystallographic tetrahedral holes now host ring CPs at their center and bond CPs along their edges. The cage CPs of this topology are internal to the Wigner-Seitz cell and are not shown. The BCC metals (columns 5 and 6) obviously possess only the BCC electron density topology, with ring CPs at the tetrahedral holes. When forced BCC, both the *l*HCP and FCC transition metals (columns 7 – 11) share the same topology, with a bond CP in the center of the octahedral hole, indicative of second neighbor bond paths, which along with the first neighbor bond paths requires cage CPs at the center of the tetrahedral holes.

Subtle difference between the electron density of the *l*HCP and FCC metals forced BCC may be discerned through comparison of electron density geometries.[1] A convenient approach to facilitate such comparisons is to borrow from band theory and construct "electron density bands" by plotting the real space electron density along high symmetry directions. Such plots are shown in Figure 4 for representative metals of the 4*d* series. The

[1] Electron (charge) density topology is a well known, and arguably abused term in chemical literature. The mathematical field of topology refers to the connectivity of a space, while geometry implies the existence of a metric. In the case of chemical analysis, electron density topology rigorously refers to the connection of critical points by critical paths and surfaces, while electron density geometry implies the ability to compare charge densities with the same topology by comparing the distances between points, paths, surfaces or other geometric properties such as curvature etc.

Preprints (www.preprints.org) | NOT PEER-REVIEWED | Posted: 22 July 2021 doi:10.20944/preprints202107.0512.v1

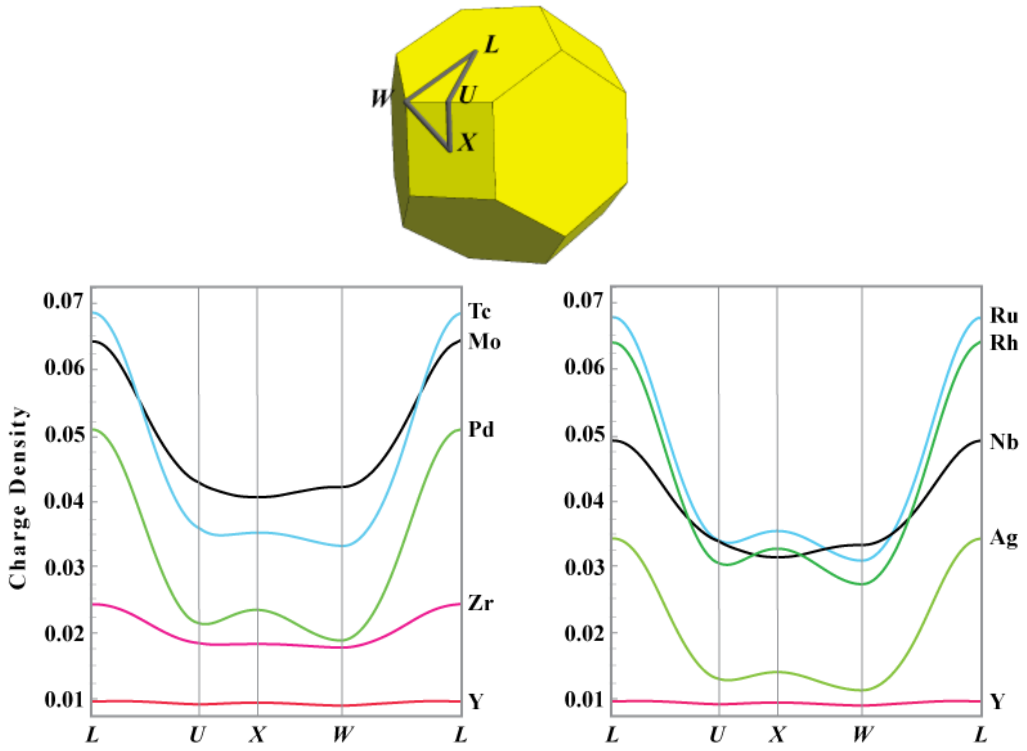

Figure 4. The electron density in AU using the LASTO software package for the 4*d* transition metals around the *L–U–X–W–L* loop. Only for Mo and Nb (representative of the non-magnetic BCC metals) is the electron density at the *W* point other than a minimum around this circuit. The graphs were divided into two sets only to enhance readability.

5*d* series shows identical topological trends. The point midway between first neighbor atoms is designated as the *L* point. The center of the BCC octahedral and tetrahedral holes are the *X* and *W* points respectively, and the electron density is shown around the circuit connecting the *L, X, W, and L* points.

As is clear from topological considerations alone, the *X* point is a minimum around the loop only for those metals for which the ground state structure is BCC. However, the electron density geometry reveals that as one proceeds across the transition metal series, additional density from added electrons is preferentially accumulated at the *X* point. In fact the electron density difference between the *X* and *W* points serves as a measure of the "proximity" to a BCC transition. Only for the stable BCC metals is this difference negative. For those metals for which there is a stable high pressure or temperature BCC phase (e.g., Ti and Zr) this difference is positive but small. The difference increases across the series with a smaller positive value for *l*HCP than FCC transition metals.

The pattern of increasingly deeper cage CPs at tetrahedrally coordinated sites while moving from left to right across the transition metal series is repeated for forced FCC structures. Again using the 4*d* series to illustrate, Figure 5 depicts the electron density around a loop on the surface of the FCC Wigner-Seitz cell for selected metals.

Unlike the forced BCC structures, the character of the CPs at the high symmetry points is the same for all metals, with the possible exception of the *e*HCP metals where the electron density is too flat for conclusive identification. The *N–H–P–N* loop passes through a bond CP, a cage CP at the octahedral hole, another cage CP at the tetrahedral hole, and returns to the bond CP. The character of the CPs around this loop requires a ring CP somewhere along the *P-H* connection, which occurs where the electron density along this line achieves it maximum value.

Preprints (www.preprints.org) | NOT PEER-REVIEWED | Posted: 22 July 2021 doi:10.20944/preprints202107.0512.v1

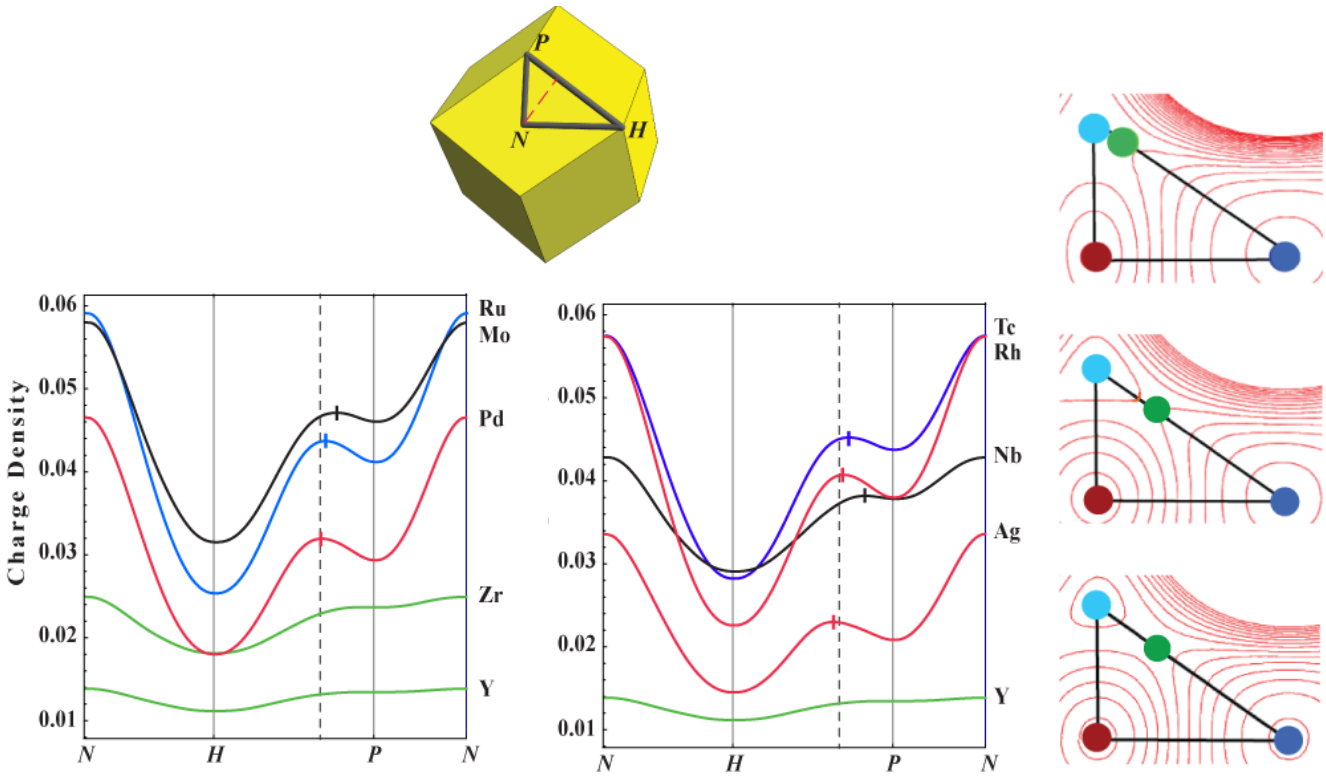

Figure 5. (left) The electron density in AU as generated using the LASTO software package for the 4*d* metals around the *N*–*H*–*P*–*N* loop. The required ring CP between the octahedral and tetrahedral cage CPs is located at the electron density maximum along the *H*–*P* loop segment and is designated with a cross. The 4*d* metals show identical trends. For the stable FCC metals this ring CP is located very near the dashed line designating its ideal position for an FCC transition metal crystal. (right) The position of the ring CP (green disks) may also be discerned from the contour graphs of the electron density in the appropriate face of the Wigner-Seitz cell for forced FCC : (from top to bottom) V, Cu, and Ir. The graphs were divided into two sets only to enhance readability.

Inspection of Figure 5 reveals that for the early transition metals this point lies close to (or on) the tetrahedral hole (*P*) and moves toward the octahedral hole (*H*) for transition metals in progressively higher columns of the periodic table. For non-magnetic transition metals with a stable FCC structure, the ring CP is very close to the center point of the flat triangular face shared by a regular octahedron centered on *H* and a regular tetrahedron centered on *P*. This particular FCC geometry we designate as "ideal', Figure 6. For all transition metals for which the FCC structure is not the stable ground state, the ring CP is located at the center of a bowed triangular face shared by a concave tetrahedron and convex octahedron. This shared face is the ring separating the octahedral and tetrahedral regions of the FCC structure. Though not shown, the same is true for BCC metals forced HCP–the HCP octahedra are convex polyhedra while the tetrahedra are not.

It appears that each of the transition metal crystallographic structures arise in response to preferred electron density topologies and geometries. For example, the presence of a bond CP at the center of the BCC octahedral hole is indicative of an instability, as is a concave tetrahedral cage in an FCC structure. Obviously, these empirically determined relationships between the structure of the electron density and crystallographic structure must have an underlying energetic origin.

4. Discussion

We begin our search for these energetic origins by noting that the electron density of an atomic system can be written as a sum over a set Kohn-Sham orbitals, ϕ_i, employing

Preprints (www.preprints.org) | NOT PEER-REVIEWED | Posted: 22 July 2021 doi:10.20944/preprints202107.0512.v1

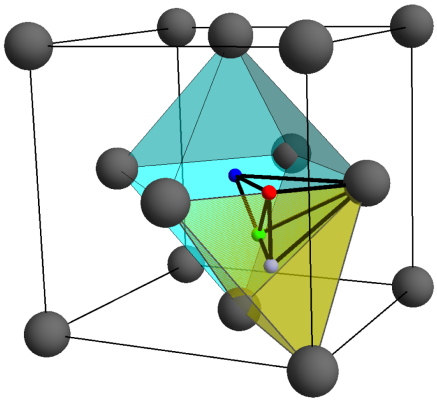

Figure 6. The ideal FCC geometry will be characterized by regular octahedra (turquoise) and tetrahedra (yellow) sharing necessarily flat faces. It is the position of the ring CP that mediates the deviation of an FCC structure from ideality. Transition metals that do not form the FCC structure, when forced, show large deviations from ideally.

any functional for exchange and correlation, a set that will be referred to here as molecular orbitals, MOs. Then,

$$\rho(x) = \sum_i n_i \phi_i(x) \phi_i(x) = \sum_i \rho_i(x) \tag{1}$$

where n_i is the occupation of orbital i and $\rho_i(x)$ is obviously the contribution to the electron density from MO i. As has been shown elsewhere [40], the kinetic energy (T) of the system at a point x can then be expressed as,

$$T(x) = L(x) + G(x) \tag{2}$$

where

$$L(x) = -\tfrac{1}{4}\nabla^2 \rho(x) \tag{3}$$

and

$$G(x) = \tfrac{1}{8} \sum_i \frac{\nabla \rho_i(x) \cdot \nabla \rho_i(x)}{\rho_i(x)} = \frac{1}{2} \sum_i n_i \nabla \phi_i(x) \cdot \nabla \phi_i(x) \tag{4}$$

The first term of Equation 2 indicates that there is a contribution to the kinetic energy at a point from the Laplacian of the electron density (its total curvature) at this point. Thus, in the region around a cage CP, for example, $L(x)$ will be negative and act to decrease the kinetic energy. On the other hand, near nuclear or pseudo-atom CPs this term will act to increase $T(x)$.

The second term arises through the gradient of the MOs from which the electron density is comprised. Orbitals that are more rapidly varying will contribute more to the kinetic energy, which indicates that anti-bonding orbitals will increase $K(x)$ and contribute the greatest increase near interatomic nodes where ϕ_i varies most rapidly.

Equation 2 is independent of the virial theorem, which for an atomic system where no forces are acting requires twice the average kinetic energy ($\overline{T}$) to equal minus the average potential energy ($\overline{V}$), i.e.,

$$2\overline{T} = -\overline{V}. \tag{5}$$

From which it follows,

$$E = \overline{T} + \overline{V} = -\overline{T}. \tag{6}$$

Leading to the seemingly contradictory conclusion that a system with the larger kinetic energy will be the more stable.

Preprints (www.preprints.org) | NOT PEER-REVIEWED | Posted: 22 July 2021 doi:10.20944/preprints202107.0512.v1

Of note, the virial theorem is not necessarily valid for arbitrarily partitioned subsystems. That is, over individual regions of an arbitrarily partitioned atomic system the virial theorem need not hold. But, over nuclear CP centered Wigner-Seitz cells, and cage CP centered electronic basins, the virial theorem is strictly obeyed [5].

Accordingly, we exploited this fact to determine how the energy of the FCC structures of Figure 5 is distributed between tetrahedral and octahedral electronic basins. This distribution is depicted in Figure 7 for the second row transition metals Mo through Ag. Calculating this distribution for the metals Y, Zr and Nb was complicated by technical issues related to non-nuclear maxima and highly curved ring surfaces.

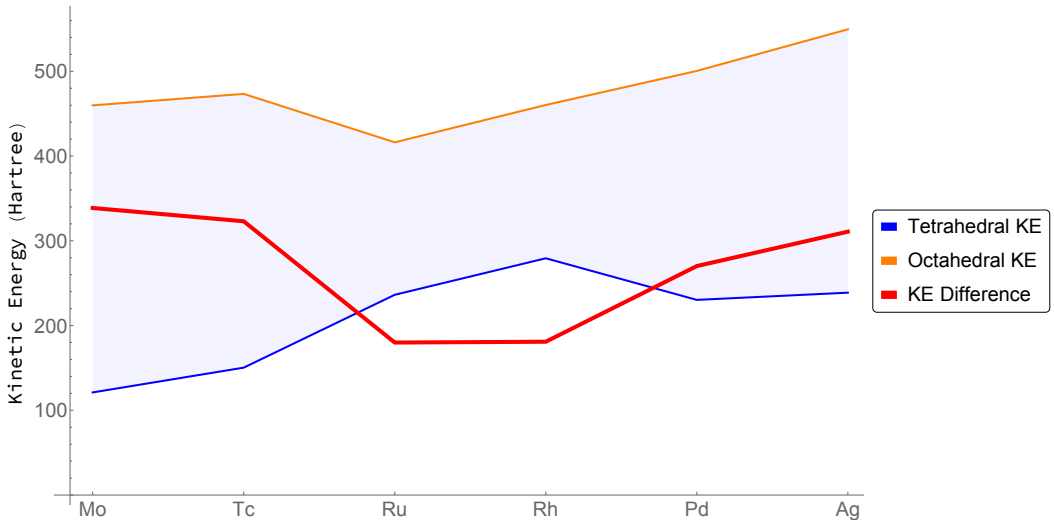

Figure 7. Integrated kinetic energy density (Hartree) in the Tetrahedral (Blue) and Octahedral (Orange) hole, and their difference (Shaded and Red).

Nonetheless, the figure reveals how the kinetic energy and hence total energy is partitioned within the FCC Wigner-Seitz cell for both transition metals that are unstable and stable in this structure. As we move from Mo to Ru, unstable as FCC, the tetrahedral hole preferentially gathers kinetic energy (lowering total energy), while the difference between energy of the octahedral and tetrahedral cages decreases, reaching a minimum at Ru. For the stable FCC structures beyond Ru—Rh, Pd and Ag—it is the octahedral hole that preferentially gathers kinetic energy, while the kinetic energy of the tetrahedral hole decreases.

We recognize a quantity M—qualitatively related to the electronic chemical potential of an electronic basin—giving the change in the total energy of the basin as one adds electrons while proceeding across a row of the periodic table. This is not identical to the electronic chemical potential, however, as that quantity is rigorously defined as the change in energy with respect to the number of electrons at constant external potential. Still, we see that for the stable FCC structures $M_o > M_t$, where the subscripts o and t denote the octahedral and tetrahedral electronic basins receptively, while for those structures that are unstable as FCC, the situation is reversed and $M_o < M_t$. Quite simply, stable FCC transition metals gain the greatest part of their stability by attracting electron density to octahedral holes.

We may infer why this is the case by appealing to Ruedenberg's variational analysis of the the virial theorem [41]. Ruedenberg notes

> There exists a variational tug-of-war between what we may call the variational electrostatic potential pull and the variationally resisting kinetic pressure.

It is this antagonistic response of potential and kinetic energy that results in a ground state structure. Specifically: assuming a trial function where $\overline{T} < -\frac{\overline{V}}{2}$, the total system energy can be variationally lowered by concentrating more density *into regions of low potential*; while, where $\overline{T} > -\frac{\overline{V}}{2}$, total energy can be lowered by *removing density from these regions*.

Preprints (www.preprints.org) | NOT PEER-REVIEWED | Posted: 22 July 2021 doi:10.20944/preprints202107.0512.v1

In this context, consider crystallographic tetrahedral holes as locations where electron density is either accumulated or depleted. As has been demonstrated, proceeding from left to right across the transition metal series the electron density in regions of tetrahedral coordination varies dramatically, from regions of electron density accumulation (pseudo-atoms) to ones of electron density depletion (cage CPs). Contrast this dramatic change to that of the octahedral coordinations, which host a cage CP for all structure types. Simply, the electron density of the tetrahedral coordinations appears to drive structure.

Hence we imagine constructing Ruedenberg's trial variational functions by considering the BCC, FCC, and HCP crystallographic structures as constructed from (not necessarily regular) four-atom tetrahedral units. The trial functions may then be formed from a linear combination (Block states) of tetrahedral fragment orbitals (FOs) that are in turn derived from atomic-like orbitals centered on tetrahedral vertices. Since in the solid state there is approximately one *s*-electron per transition metal, the electron density variations across the TM series result primarily from varying occupation of twenty tetrahedral FOs built from *d*-atomic orbitals, each of which can be written as the product of an angular and a radial part.

These twenty FOs can be placed into four classes distinguished by their net number of bonding interactions (Figure 8), which will correlate with their gradient contributions to the electron density. In the first class are those orbitals characterized by bonding interactions along each of the six tetrahedral edges, possessing a net bond order of six. In the second class are orbitals that are anti-bonding along two opposite tetrahedral edges and bonding along the remaining four, with a net bond order of two. The third class is bonding along two edges and anti-bonding along four edges (bond order -2). Finally the fourth class is distinguished by orbitals that are anti-bonding along all edges (bond order -6).

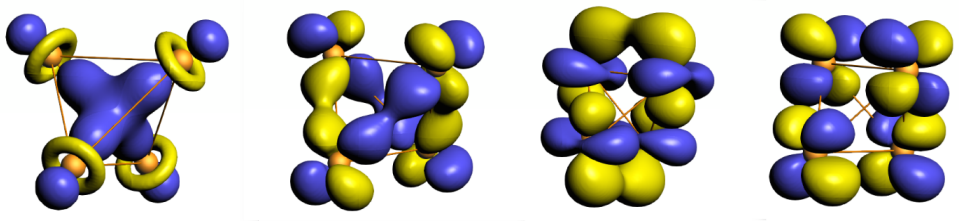

Figure 8. Examples from each class of *d*-derived tetrahedral FOs. From left to right tetrahedral orbital that are: a class I FO that is a mixture of σ and π bonding along each tetrahedral edge giving a FO bond order of 6; a class II FO that is σ bonding along four edges and weakly δ anti-bonding along two edges with a bond order of 2; a class III FO that is δ bonding along two edges and π anti-bonding along four edges with a bond order of -2; and a class IV FO that is δ anti-bonding along two edges and π anti-bonding along four edges with a bond order of -6

For all molecules and materials the first electronic states filled are those that are most bonding while the last filled are the most anti-bonding. Hence, for the transition metals, the first states to be occupied—those at the bottom of the *d*-band—will be formed from a linear combination of FOs drawn from class I; and the last occupied—those at the top of the *d*-band—will be formed from a linear combination of FOs drawn from class IV. Midband states will be formed from a linear combination of class II and III FOs, with a greater contribution from class III FOs as one move up the *d*-band. Quite generally–and entirely consistent with the calculated values of kinetic energy shown in Figure 7–the gradient contributions to the kinetic energy, particularly from the tetrahedrally coordinated region, will increase across the transition metal series—smaller for the early transition metals where class I FOs dominate, but substantial for late transition metals where class IV FOs are occupied.

Let us imagine employing as our trial variation function the true ground state wave function for a midband transition metal say Rh. Using this trial wave function for all the elements to the left of Rh, $\overline{T} < -\frac{\overline{V}}{2}$ and thus relative to the Rh, the charge density will expand into the tetrahedral hole as a means of variationally lowering the total system energy. This expansion leads to the bond point in the center of tetrahedral coordinations

Preprints (www.preprints.org) | NOT PEER-REVIEWED | Posted: 22 July 2021 doi:10.20944/preprints202107.0512.v1

for the *e*HCP metals, ring points for the BCC metals, and as we will see, face sharing of tetrahedra for the late *l*HCP metals. All of this is entirely consistent with the observed structural trends. Now as per Ruedenberg's argument, for the elements to the right of Rh, $\overline{T} > -\frac{\overline{V}}{2}$. Now system energy may be lowered by contracting the radial part of the trial functions and thus, relative to Rh, removing density from the tetrahedral holes, resulting in deeper cages, as confirmed by inspection of Figure 5. The removal of charge from the tetrahedral and octahedral holes is realized by shifting density toward the nucleus.

In accordance with the virial theorem, the increasing contributions to the kinetic energy from tetrahedral coordinations across the transition metal series must be offset by decreases to the potential energy. Potential will be most effectively decreased by charge transfer to the tetrahedral hole, consistent with our observation that early in the series $M_o < M_t$, charge is transferred from octahedra to tetrahedra as a means of both increasing kinetic energy and decreasing potential energy. At the same time, this electron density depletion at the octahedral center yields the cage CP topologically required of extended systems.

A further lowering of potential (increasing of kinetic energy) is realized in the *e*HCP structure through tetrahedral face sharing to produce atomically dense five atom trigonal bi-pyramids hosting pseudo-atom CPs. Comparatively flat charge densities distributes the electron density across these bi-pyramids and minimizes the offsetting effects of electron-electron repulsion. The accumulation of density in the tetrahedra and its depletion from the center of the octahedra yields a steeper electron density and an increase in the average kinetic energy of the octahedral basin.

A key point here is that early in the transition metal series energy lowering is achieved through the redistribution of electronic charge from octahedral to tetrahedral coordinations. For the late transition metals the situation is quite different.

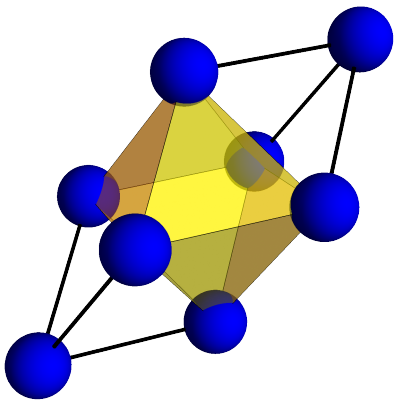

Figure 9. The octahedral coordination may be built from tetrahedra decorating the opposite faces of an octahedron.

As a means of rationalizing these differences, consider that an octahedral coordination may be formed from two tetrahedra "decorating" opposite triangular faces of an octahedron (Figure 9). The octahedral electron density may now be thought of as arising from forty FOs, resulting from the bonding (in phase) and antibonding (out of phase) combination of our twenty tetrahedral FOs. The antibonding FOs must possess an interatomic node and hence a steep gradient normal to the nodal plane passing through the octahedral center. As these antibonding orbitals are filled, the contributions to the kinetic energy from the octahedral cage will increase. Inspection of Figure 7 indicates that this process begins with group 9 elements (*e.g.* Ru) and culminates with the complete filling of the *d*-band.

The virial theorem requires that this kinetic energy increase be accompanied by a potential energy decrease. However, unlike the early transition metal, where the tetrahedral coordination was available to receive density, this is no longer the case. The center of the

Preprints (www.preprints.org) | NOT PEER-REVIEWED | Posted: 22 July 2021 doi:10.20944/preprints202107.0512.v1

tetrahedral coordination now host a deep cage that contributes to the kinetic energy of the system. The late transition metals resolve this situation through variations in the radial part of our trial variational functions.

We recognize two electron density regions around every atom: an atom like or near nuclear region where the gradient of the electron density is essentially radial, and an interatomic region where the electron density gradient has a substantial tangential component [42,43]. While it is tempting to associate these regions with the more common core and valence regions of traditional chemistry, such an association is not appropriate. First, because core and valence are only well-defined within an MO representation of structure and do not have clear density based analogues, and second, related to the first, even valence orbitals contribute density to the atom like regions near the nucleus.

With this identification we can clearly articulate the differences between the early and late transition metals. The early transition metals satisfy the virial theorem through the redistribution of charge within the interatomic region while the late transition metals do so by redistributing charge from the interatomic region to the near nuclear region. In the latter case, this redistribution results in an expansion of the atom like region at the expense of the interatomic region. Between the *e*HCP transition metals where stability stems from potential lowering in tetrahedra, and the late FCC transition metals where stability is promoted by kinetic energy increase in both the tetrahedral and octahedral cages, are the BCC and *l*HCP structures where potential decreases achieved through the concentration of charge are nearly balanced by those of depleting density and increasing kinetic energy. The force driving the distortion of BCC tetrahedra is clearly evident in the competition between charge transfer to tetrahedra, and charge redistribution within tetrahedra. As demonstrated, BCC metals forced FCC host a cage CP at the center of their tetrahedral coordinations. In their more stable BCC form, these coordinations host a ring CP (Figures 5 and 4).

Consider then an FCC to BCC transformation that manifests through a lengthening of two opposite edges of a tetrahedron and simultaneously shortening of the remaining four edges. The contributions to $G(x)$ from MOs that include contributions from class II FOs that are anti-bonding along the two lengthening edges and bonding along the shortening edges (Figure 8) will diminish through this distortion, lessening the depth of the tetrahedral cage point and making $L(x)$ at the tetrahedral cage CP less positive. If the cage is not too deep, the tetrahedral coordination will be transformed from a source to a sink for electron redistribution. Much as in the case of the *e*HCP structure, charge is redistributed from the octahedral cage to the tetrahedral coordination—in this case to its ring and bond CPs where the potential is lower. Diminished charge at the octahedral cage CP and elevated charge in the bond and ring CPs produces a more rapidly varying electron density across the BCC octahedral electron basin and hence increases its kinetic energy.

Contrast this behavior to that of an FCC metal forced BCC, its electron density topology is produced by cage centered distorted tetrahedra sharing faces. Where the stable BCC topology hosts a cage CP at the octahedral center, the FCC forced BCC topology hosts a shallow bond-CP. Because $L(x)$ at the tetrahedral center is more positive than its value at the bond CP at the octahedral center, charge will be redistributed from the tetrahedron to the octahedron, inducing a distortion that takes the structure back to FCC. The resulting FCC electron density is more rapidly varying across the octahedral and tetrahedral cages than it was through the tetrahedral cages of the FCC forced BCC structure. Again consistent with the fact that more stable structures is the one with the greater kinetic energy.

The key point: BCC stability is a consequence of charge redistribution from octahedra to the ring structures of tetrahedral faces. The restriction for BCC stability is that a cage CP at the center of regular FCC tetrahedra must be shallow. If this is not the case, there will be insufficient charge transfer to transform the cage to a ring CP and $L(x)$ will be of the wrong sign to promote charge transfer between the octahedral and tetrahedral coordinations.

The factors stabilizing *l*HCP over FCC are more subtle than those driving the BCC structure. Still the mechanism is consistent with the overall pattern of charge transfer from

Preprints (www.preprints.org) | NOT PEER-REVIEWED | Posted: 22 July 2021 doi:10.20944/preprints202107.0512.v1

octahedral to tetrahedral coordinations. Unlike the BCC structure, the magnitude of the charge redistribution is insufficient to transform the tetrahedral cage CP.

The magnitude of the charge redistribution can be inferred from the density distribution plots of Figure 10, which show the relative volumes of the Wigner-Seitz cell occupied by a given density. These plots depict the change of the density distribution for Pd, Rh, Ru, and Tc between FCC and HCP with an ideal $\frac{c}{a}$. Of particular note, the electron density distribution changes little when the normally FCC metals (Rh and Pd) are forced HCP. On the other hand, there is a substantive change in the density distribution of the HCP metals (Tc and Ru) when forced FCC. Electron density that was deep in the octahedral cage is shifted to the tetrahedral cage and particularly into the rings and bond paths forming their edges and faces. The density becomes steeper in the octahedral cage particularly in the direction of the c lattice vector. Apparently the lower symmetry about the tetrahedral and octahedral cages of HCP compared to FCC allows the charge redistribution. In the absence of charge redistribution, the FCC structure is preferred simply because the strong electron electron repulsion is minimized by vertex sharing and hence maximizing the distance between the electron rich faces and bonds of the tetrahedral cages.

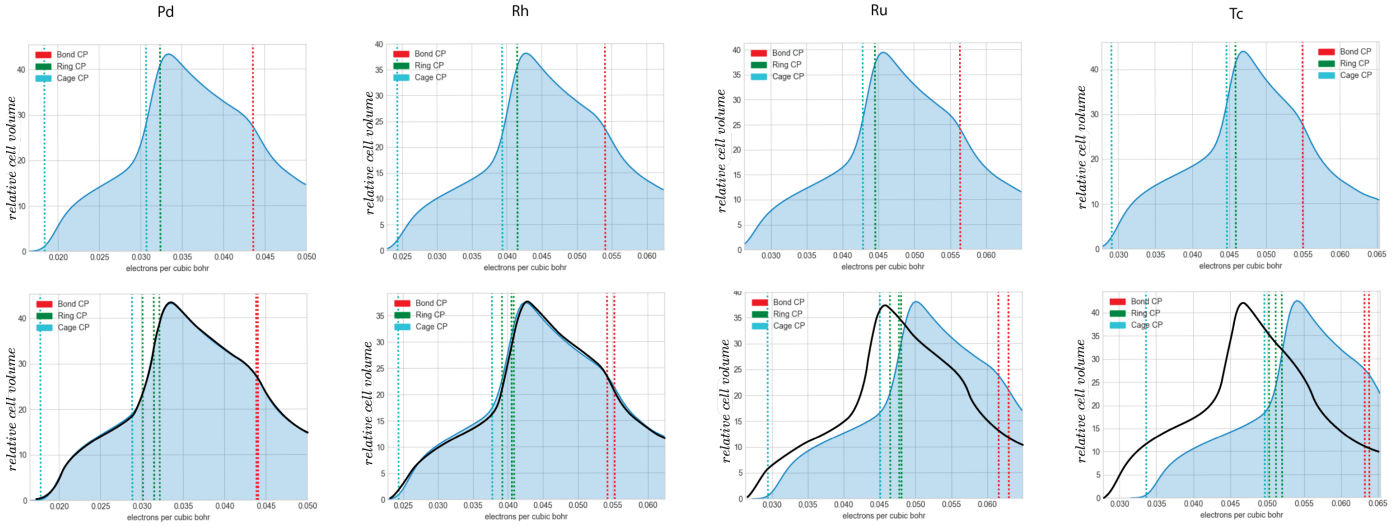

Figure 10. In arbitrary units the relative fraction of the Wigner-Seitz cell occupied by a given density, i.e. the density distribution, accompanying an FCC to HCP transformation. The top row shows the electron density distribution of the FCC structure and the second row is the distribution of the HCP structure. The normally FCC metals Rh and Pd experience very little charge redistribution through the transformation. For the normally HCP metals, however, charge is observed to be transferred to the bonds and rings of the shared tetrahedral–octahedral faces, making the electron density in the octahedral cage steeper and hence increasing its kinetic energy. The small tails which lie at densities below the cage CPs are fitting artifacts.

The charge rearrangement attendant with the transformations of FCC to BCC and *l*HCP are consistent with those of Jahn-Teller transformations. While the exact details of these transformations can be more easily extracted from an orbital perspective (see [44]) at the moment, other than a "not too deep tetrahedral cage" it is not possible to pinpoint where in the electron density the incipient orbital instability lies.

5. Conclusion

We have employed the conceptual and theoretical framework of molecular chemistry in an attempt to rationalize the HCP, BCC and FCC crystallographic structures of the nonmagnetic elemental transition metals. Specifically, we have drawn on concepts from the quantum theory of atoms in molecules, the molecular virial theorem, and frontier orbital theory to develop a chemically based fundamental understanding of the evolution of electron density topology and geometry as one proceeds from left to right across the transition metal series. As a marked departure from conventional metallurgical approaches,

where structure is described as the packing of local tetrahedral and octahedral atomic coordinations, we take a broader look at structure by describe it as arising from the packing of topological units characterized by electron density minima at their center.

While the electron density and metallurgical approach lead superficially to the same structural representation for the late transition metals, the electron density approach leads to a chemically nuanced understanding of the early transition metals. In particular, the structure of the electron density of the early transition metals may be seen to be a consequence of bonding interactions between tetrahedral coordinations. On the other hand, the structure of the late transition metals, results from antibonding interactions between the same units. The crystallographic structures between the early and late transition metals can then be rationalized as resulting from mixed bonding/antibonding character, where the preferred structures are those for which the interatomic distance in antibonding directions is lengthened.

Though here we investigated only the nonmagnetic transition metals, the approach is sufficiently general and is applicable to more complex alloys. The challenge is identifying the relevant topological units and then cataloguing the possible interactions between these units. As an example, we previously brought this methodology to bear in a study of the structure of metallic glasses [45]. Though complex and confronted with difficulties, the approach allows for a more direct application of chemical formalism. Perhaps the chemical insights that are forthcoming will prove useful in the ongoing effort to design metals and alloys.

Author Contributions: Conceptualization, S.R. and M.E.; methodology, S.R, T.W., M.R and M.E.; software, T.W.; formal analysis, S.R.; writing—original draft preparation, S.R.; writing—review and editing, S.R, T.W, M.R and M.E.; funding acquisition, M.E. All authors have read and agreed to the published version of the manuscript.

Funding: Support of this work under ONR Grant Nos. N00014-16-1-2581 and N00014-20-1-2794 is gratefully acknowledged.

Conflicts of Interest: The authors declare no conflict of interest.

References

1. Pauling, L., The Nature of the Chemical Bond. *JACS* **1931**, *53*, 1367–1400.
2. Fukui, K.; Yonezawa, T.; Shingu, H., A Molecular Orbital Theory of Reactivity in Aromatic Hydrocarbons. *J. Chem. Phys.* **1952**, *20*, 722–725.
3. Hoffmann, R.; Woodward, R. B., Conservation of Orbital Symmetry. *Accounts of Chemical Research* **1968**, *1*, 17–22.
4. Hammond, G. S., A Correlation of Reaction Rates. *JACS* **1955**, *240*, 145–159.
5. Bader, R. F. W., *Atoms in Molecules: A Quantum Theory*. Claredon Press: Oxford, UK, 1990.
6. Lewis, G. N., The Atom and the Molecule. *JACS* **1916**, *38*, 762–785.
7. Lewis, G. N., *Valence and the Structure of Atoms and Molecules.* The Chemical Catalogue Company: New York, 1923.
8. Taylor, G. I., The Mechanism of Plastic Deformation in Crystals. Part I. Theoretical. *The Royal Society* **1934**, *145*, 362–387.
9. Orowan, E., Zur Kristallplastizität. I. *Z. Physik* **1934**, *89*, 605–613.
10. Polanyi, M., Über eine Art Gitterstörung, die einen Kristall plastisch machen könnte. *Z. Physik* **1934**, *89*, 660–664.
11. Hohenberg, P.; Kohn, W., Inhomogeneous Electron Gas. *Phys. Rev.* **1964**, *136*, B864–B871.
12. Pettifor, D. G., Electron Theory in Materials Modeling. *Acta Materialia* **2003**, *51*, 5649–5673.
13. Raju, S.; Mohandas, E.; Raghunathan, V.S., Engel-Brewer Electron Correlation Model: A Critical Discussion and Revision of Concepts. Materials Transactions *JIM* **1996**, *37*, 195–202.
14. Pauling, L., The Nature of the Interatomic Forces in Metals. *Phys. Rev.* **1938**, *54*, 899–904.
15. Pauling, L., A Resonating-Valence-Bond Theory of Metals and Intermetallic Compounds. *The Royal Society* **1949**, *196*, 343–362.
16. Altmann, S. L.; Coulson, C. A.; Hume-Rothery, W., On the Relation between Bond Hybrids and the Metallic Structures. *The Royal Society* **1957**, *240*, 145–159.
17. Hume-Rothery, W., The Engel-Brewer Theories of Metals and Alloys. *Progress in Materials Science* **1968**, *13*, 229–265.
18. Hume-Rothery, W., A Note on the Engel-Brewer Theory of Metallic Structures. *Acta-Metallurgica* **1965**, *13*, 1039–1042.
19. Tiwari, G.P.; Ramanujan, R. V., Review: The Relation between the Electron to Atom Ratio and Some Properties of Metallic Systems. *Journal of Mat. Sci.* **2001**, *36*, 271–283.
20. Milnor, J., *Morse Theory*. Princeton University Press: Princeton, NJ, 1963

21. Matta, C. F; Boyd, R. J.,*The Quantum Theory of Atoms and Molecules: From Solid State to DNA and Drug Design*. Wiley-VCH & Co. KGaA: Weinheim, 2007.
22. Besnainou, S.; Roux, M.; Daudel, R., Retour Sur Leffet de la Liaison Chimique sur la Densite Electronique. *C.R. Acad Sci.* **1955**, *241*, 311–313.
23. Bersuker, G. I.; Peng, C,; Boggs, J. E. The Nature of the Covalent Bond - The Existence and Origin of Nonnuclear Attractors. *J. Phys. Chem*. **1993**, *97*, 9323–9329.
24. Zou P. F.; Bader, R. F. W., A Topological Definition of a Wigner-Seitz Cell and the Atomic Scattering Factor. *Acta Crystallographica A*. **1994**, *50*, 714–725.
25. Jones, T. E.; Eberhart, M. E., The Topologies of the Charge Densities in Zr and Ru. *Acta. Crystallographica A*,**2009**, *A65*, 229–265.
26. Bader, R. F. W., Bond Paths are not Chemical Bonds. *J. Phys. Chem. A.* **2009**, *113*, 10391–10396.
27. Castillo, N.; Matta, C.; Boyd, R. J., The First Example of a Cage Critical Point in a Single Ring: A Novel Twisted α Helical Ring Topology. *Chemical Physics Letters* **2005**, *409*, 265–269.
28. Pendás, A. M; Aurora, C.; Víctor, L., Ions in Crystals: The Topology of the Electron Density in Ionic Materials I. Fundamentals. *Physical Review B* **1997**, *50*, 4275–4284.
29. Eberhart, M. E., A Quantum Description of the Chemical Bond. *Philosophical Magazine B*. **2001**, *81*, 721.
30. Jones, T. E.; Eberhart, M. E., The Bond Bundle in Open Systems. *International Journal of Quantum Chemistry* **2010**, *110*, 1500–1505.
31. te Velde, G.; Baerends, E. J., Precise Density-Functional Method for Periodic Structures. *Phys. Rev. B* **1991**, *44*, 7888.
32. BAND 2020, SCM, Theoretical Chemistry, Vrije Universiteit, Amsterdam, The Netherlands. Available Online: http://www.scm.com.
33. Kresse, G; Furthmuller, J., Efficiency of Ab-initio Total Energy Calculations for Metals and Semiconductors using a Plane-Wave Basis Set. *Computational Materials Science*, **1996**, *6*, 15–50.
34. Kresse, G; Furthmuller, J., Efficient Interactive Schemes for Ab-initio Total-Energy Calculations Using a Plane-Wave Basis Set. *Phys. Rev. B.*, **1996**, *54*, 11169–11186.
35. Davenport, J. W., Linear Augmented-Slater-Type-Orbital Method for Electronic-Structure Calculations. *Phys. Rev. B.*, **1984**, *29*, 2896–2904.
36. Vosko, S. H.; Wilk, L.; Nusair, M., Accurate Spin-Dependant Electron Liquid Correlation Energies for Local Spin-Density Calculations – A Critical Analysis. *Canadian Journal of Phyisics*, **1980**, *58*, 1200–1211.
37. van Lenthe, E.; Ehlers, A.; Baerends, E., Geometry Optimizations in the Zero Order Regular Approximation for Relativistic Effects. *J. Chem. Phys.*, **1999**, *110*, 8943–8953.
38. Wilson, T. R.; Rajivmoorthy, M.; Goss, J.; Riddle, S. K.; Eberhart, M. E., Observing the 3D Chemical Bond and its Energy Distribution in a Projected Space. *Chem. Phys. Chem.*, **2019**, *20(24)*, 3289–3305. Available: https:// github.com/ moltheorygroup/ BondalyzerTecplotAddon/ releases
39. Tecplot 360 2013R1. Tecplot Inc. https://www.tecplot.com, 2013.
40. Bader, R. F. W.; Preston, H. T. J., The Kinetic Energy of Molecular Charge Distributions and Molecular Stability. *International Journal of Quantum Chemistry*, **1969**, *3*, 327–347.
41. Ruedenberg, K.; Schmidt, M. W., Physical Understanding Through Variational Reasoning: Electron Sharing and Covalent Bonding. *J. Phys. Chem* **2009**, *113*, 1954–1968.
42. Wilson, T. R.; Eberhart, M. E., Quantum Theory of Atoms in Molecules in Condensed Charge Density Space. *Canadian Journal of Chemistry*, **2019**, 1–6.
43. Eberhart, M. E.; Jones, T. E., Cauchy Pressure and the Generalized Bonding Model for Nonmagnetic BCC Transition Metals. *Physical Review B*, **2012**, *86*, 134106.
44. Lee, S.; Hoffmann, R., BCC and FCC Transition Metals and Alloys: A Central Role for the Jahn-Teller Effect in Explaining their Ideal and Distorted Structures. *JACS*, **2002**, *124*, 4811–4823.
45. Jones, T. E.; Miorelli, J.; Eberhart, M. E., Reactive Cluster Model of Metallic Glasses. *J. Chem. Phys.*, **2014**, *140*.